



Fouling effect on the resistance of different ship types

Soonseok Song^{a,*}, Yigit Kemal Demirel^a, Claire De Marco Muscat-Fenech^b, Tahsin Tezdogan^a, Mehmet Atlar^a

^a Department of Naval Architecture, Ocean and Marine Engineering, University of Strathclyde, 100 Montrose Street, Glasgow, G4 0LZ, UK

^b Faculty of Engineering, University of Malta, Msida, MSD2080, Malta

ARTICLE INFO

Keywords:

Biofouling
Ship resistance
KRISO container Ship (KCS)
KRISO tanker (KVLCC2)
Computational fluid dynamics (CFD)

ABSTRACT

Considering that the ship hydrodynamic behaviours differ by the ship types and dimensions, the effect of biofouling on ship resistance can also vary with different ships. In this study, Unsteady Reynolds Averaged Navier-Stokes (URANS) based towed ship models were developed to simulate the roughness effect of biofouling on ship resistance. A container ship (KCS) and a tanker (KVLCC2), representing slender and a full hull forms, were modelled with various scale factors and speeds. The CFD simulations were conducted with several fouling conditions by embedding the roughness function of barnacles into the wall-function of the CFD model (i.e. modified wall-function approach). The fouling effects on the resistance components, form factors, wake fractions and the flow characteristics were investigated from the simulations. Significant differences were observed varying with the hull types, lengths (scales) and speeds of the ships and it was concluded that these differences are dominated by two parameters; relative roughness height and the roughness Reynolds number.

1. Introduction

It is well established that the power and fuel consumption of a ship increases with the hull roughness. Hull roughness can be caused by various factors including mechanical causes (e.g. mechanical damage, sand-blasting, plate waviness, welds, mechanical damage to the marine coatings), chemical and electrochemical processes (i.e. corrosion), and finally the colonisation of biofouling, which is often the most critical (Tezdogan and Demirel, 2014; Townsin, 2003). The economic and environmental problems due to the increased hull roughness include increases in ship resistance, fuel consumption and greenhouse gas emissions. The mitigation measures are also associated with costly antifouling coatings and drydocking (Schultz et al., 2011). Therefore, accurate predictions of the impact of hull roughness on ship performance are needed for the best choice of antifouling coatings and scheduling of hull cleaning (Uzun et al., 2019).

The most prevalent method for predicting the roughness effect on ship resistance is the similarity law scaling of Granville (1958, 1978), which has been widely used over the decades by many researchers (Schultz, 2002, 2004; Schultz and Flack, 2007; Flack and Schultz, 2010; Schultz et al., 2011; Demirel et al., 2017a, 2019; Li et al., 2019; Uzun et al., 2020). However, this scaling method has several disadvantages as criticised by Demirel et al. (2017b). The most critical one is that, in this

method, the frictional resistance of the rough hull is assumed to be equal to that of an equivalent length flat plate, and hence the three-dimensional (3D) effects are discarded. Accordingly, this method cannot predict the roughness effect on other ship resistance components which are closely related to the 3D hull shapes. Another arguable simplification is the uniform and constant distribution of the roughness Reynolds number, k^+ , and roughness function, ΔU^+ , along with the whole flat plate, which is not the case in the real world.

On the other hand, there have been active efforts to model the roughness effect using Computational Fluid Dynamics (CFD). The advantage of using CFD is that the above-mentioned demerits of Granville's flat plate approach can be avoided. In CFD simulations, the 3D effects can be taken into account and the simulations are free from the scale effect once they are modelled in full-scale. Also the local friction velocity, u_τ , is dynamically computed for each discretised cell in the simulations, and therefore the dynamically varying roughness Reynolds number, k^+ , and corresponding roughness function, ΔU^+ , can be considered in the computations (Atlar et al., 2018).

Accordingly, there have been recent studies using CFD simulations to investigate the roughness effect on ship resistance (e.g. Demirel et al., 2014; Demirel et al., 2017b; Farkas et al., 2018; Farkas et al., 2019; Song et al., 2019a) and propeller performance (Owen et al., 2018; Song et al., 2019b, 2020a), as well as ship self-propulsion characteristics (Song

* Corresponding author.

E-mail address: soonseok.song@strath.ac.uk (S. Song).

et al., 2020b; Farkas et al., 2020a). Recently, Song et al. (2020c) extended the validation of the roughness modelling in CFD by comparing their method, which had been only validated against flat plates before, with a model ship towing test of Song et al. (2020d). The findings of Demirel et al. (2017b) and Song et al. (2019a) are especially important, as their results suggest that the hull roughness does affect not only the ship frictional resistance but also the other resistance components, e.g. the viscous pressure resistance and wave-making resistance. This is certainly notable since it had been widely believed that the roughness effect on the wave-making resistance is negligible (e.g. Carchen et al., 2019). However, these findings cannot be generalised as these studies were conducted only for a single type of hull form (KCS).

Considering that the ship hydrodynamic behaviours vary with different ship types and dimensions, the roughness effect can also vary with different ship forms. Recently, Farkas et al. (2019) observed differences in the roughness effect on the form factors and the nominal wake between two different ship types (i.e. container ship and bulk carrier). Also, it is well established that the form factors of ships change by scales (García-Gómez, 2000; Min and Kang, 2010; Van et al., 2011; Dogrul et al., 2020). In this context, it is worth investigating the roughness effect on the ship hydrodynamic characteristics of different ships with variations of the scales and speeds.

To the best of the authors' knowledge, there exists no specific study investigating the roughness effect on the ship resistance of different hull forms with different scales and speeds. Therefore, the aim of this study is to fill this gap by performing a series of CFD simulations of different hull forms in different scales and speeds. In this study, Unsteady Reynolds Averaged Navier-Stokes (URANS) based ship models of a container ship and a tanker were developed. Each vessel was modelled in three different scales, namely model-scale, moderate-scale and full-scale. The modified wall-function approach was used with the roughness function of barnacles, determined by Demirel et al. (2017a), to represent the surface roughness of barnacle fouling. The simulations of each vessel (KCS and KVLCC2) in different scales were performed with a range of speeds. Finally, the effect of biofouling on ship resistance components, form factor and flow characteristics around the hulls were investigated.

2. Background

2.1. Roughness function and modified wall-function approach

The surface roughness causes an increase in turbulence, hence the skin friction increases. The roughness effect can be observed as a downward shift of the mean velocity profile in the turbulent boundary layer. This downward shift is termed as the 'roughness function', ΔU^+ . The non-dimensional velocity profile in the log-law region for a rough surface is then given as

$$U^+ = \frac{1}{k} \ln y^+ \quad (1)$$

where U is the mean velocity at the normal distance, y , from the wall, U_τ is the friction velocity defined as $\sqrt{\frac{\tau_w}{\rho}}$, τ_w is the wall shear stress, ν is the kinematic viscosity defined as the ratio of dynamic viscosity to the fluid density, $\frac{\mu}{\rho}$, k is the von Karman constant and B is the log-law intercept.

The roughness function, ΔU^+ can be expressed as a function of the roughness Reynolds number, k^+ , defined as

$$k^+ = \frac{\kappa U_\tau}{\nu} \quad (2)$$

It should be noted that ΔU^+ simply vanishes in the case of a smooth condition.

Demirel et al. (2017a) determined the roughness function of barnacles through towing tests of a flat plate covered with artificial barnacle patches with varying sizes (small, medium and big) and coverages (10–50%). From the experimental results, they observed that the

roughness functions of the barnacles follow the Colebrook type roughness function model of Grigson (1992) as shown in Fig. 1, given by

$$\Delta U^+ = \frac{1}{\kappa} \ln(1 + \kappa^+) \quad (3)$$

In this study, three representative surface conditions (S20%, M20% and B20%) were selectively used for the simulations rather than including all the surface conditions of Demirel et al. (2017a). Table 1 shows the roughness length scales for the fouling conditions used in this study.

Recently, Song et al. (2019a) employed this roughness function into the wall-function in the CFD model and conducted simulations of a towed flat plate to validate the modified wall-function approach. The simulation results showed good agreement with the experiment of Demirel et al. (2017a). In this study, the same modified wall-function approach with the same roughness function is used to investigate the effect of barnacles on KCS and KVLCC2.

2.2. Resistance components

The total resistance, R_T , of a ship can be divided into two main components; the frictional resistance, R_F , and the residuary resistance, R_R , given by

$$R_T = R_F + R_R \quad (4)$$

The frictional resistance arises from the friction between the fluid and the hull surface while the residuary resistance is a pressure related resistance consisting of viscous pressure resistance R_{VP} , and wave-making resistance R_W , given by

$$R_T = R_F + R_{VP} + R_W \quad (5)$$

The viscous pressure or also known as form drag is broadly assumed to be proportional to the frictional resistance (Lewis, 1988), with the use of form factor, κ , as given

$$R_{VP} = \kappa R_F \quad (6)$$

$$R_T = (1 + \kappa) R_F + R_W \quad (7)$$

The resistance components can be normalised by dividing each term by the dynamic pressure, $\frac{1}{2} \rho V^2$, and the wetted surface area of the ship hull, S . The resistance coefficients can be defined as

$$C_T = C_F + C_R \quad (8)$$

$$C_T = C_F + C_{VP} + C_W \quad (9)$$

$$C_T = (1 + \kappa) C_F + C_W \quad (10)$$

where, C_T , C_F , and C_R is the coefficient of the total, frictional and residuary resistance, respectively.

3. Numerical modelling

3.1. Governing equations and physical modelling

The proposed CFD models were developed based on the unsteady Reynolds-averaged Navier-Stokes (URANS) method using a commercial CFD software package, STAR-CCM+ (version 13.06). The second-order upwind convection scheme and a first-order temporal discretisation were used for the momentum equations. The overall solution procedure was based on a Semi-Implicit Method for Pressure-Linked Equations (SIMPLE) type algorithm. The shear stress transport (SST) $\kappa - \omega$ turbulence model was used to predict the effects of turbulence, which combines the advantages of the $\kappa - \omega$ and the $\kappa - \epsilon$ turbulence model (Menter, 1994). A second-order convection scheme was used for the equations of the turbulent model. For the simulations where the free surface exists, the Volume of Fluid (VOF) method was used with

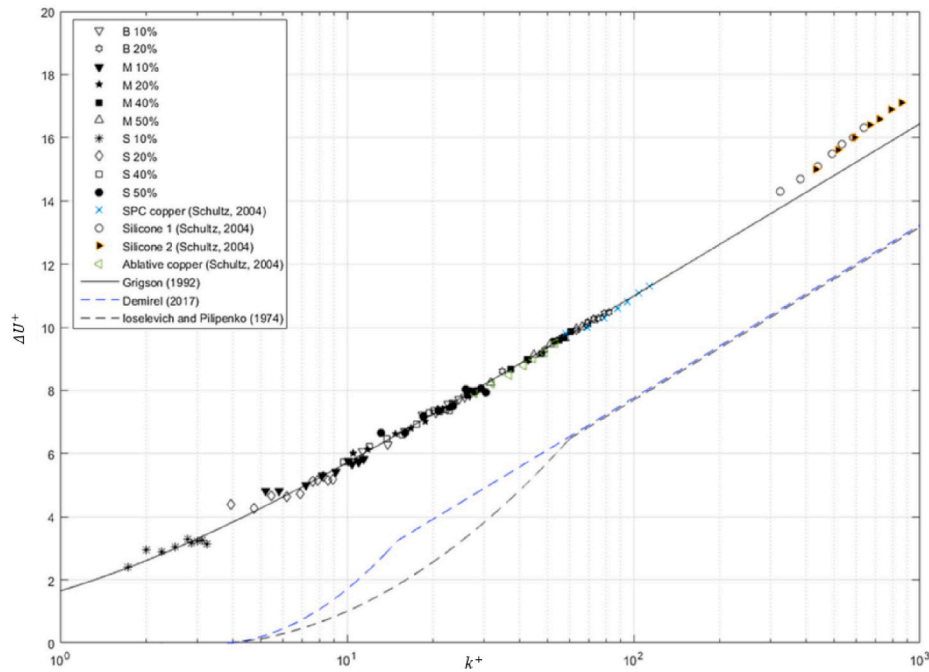


Fig. 1. Roughness functions for the fouling conditions and Colebrook type roughness function of Grigson (1992), adapted from Demirel et al. (2017a).

Table 1

Roughness length scales of the surface conditions, adapted from Demirel et al. (2017a).

| Surface condition | Barnacle type | Surface coverage,FX (%) | Barnacle height,FX (mm) | Representative roughness height, k_G (μm) |
|-------------------|---------------|-------------------------|-------------------------|--|
| S20% | Small | 20% | 1.25 | 63 |
| M20% | Medium | 20% | 2.5 | 165 |
| B20% | Big | 20% | 5 | 489 |

High-Resolution Interface Capturing (HRIC).

3.2. Geometry and boundary conditions

In order to investigate the effect of biofouling on different ships, the benchmark ship hulls of a container ship (KCS) and a tanker (KVLCC2) were used for the CFD simulations. Figs. 2 and 3 show the hull geometries of KCS and KVLCC2, respectively, while Tables 2 and 3 depict the principal particulars of these vessels. As shown in the figures and the tables, KCS represents a fast container ship with a sharp bow-shape, a slender hull form and a relatively shallow draught (i.e. $C_B = 0.65$, $F_n = 0.26$, $\frac{L_{PP}}{T} = 21.30$), whereas KVLCC2 represents a slow tanker with a fuller bow-shape and hull form and a relatively deep draught (i.e. $C_B = 0.81$, $FX = 0.14$, $FX = 15.38$).

Table 4 shows the simulation cases used in this study. Each vessel was modelled in two different computational domain types, namely double-body and free-surface models, for the purpose of decomposing the resistance components. In a double-body simulation, the free surface is replaced by the symmetry boundary condition such that there is no wave-making behaviour and hence there exist only the viscous resistance (i.e. $R_T = R_V = R_F + R_{VP}$). On the other hand, the free-surface



Fig. 2. Geometry of KCS hull with a rudder.



Fig. 3. Geometry of KVLCC2 hull with a rudder.

Table 2

Principal particulars and conditions of the KCS simulations, adapted from Kim et al. (2001) and Larsson et al. (2013).

| Main particulars | Full-scale | Moderate-scale | Model-scale |
|---|------------|----------------|-------------|
| Scale factor, λ | 1 | 10 | 31.6 |
| Length between the perpendiculars, L_{PP} (m) | 230 | 23 | 7.278 |
| Length of waterline, L_{WL} (m) | 232.5 | 23.25 | 7.358 |
| Beam at waterline, B_{WL} (m) | 32.2 | 3.22 | 1.019 |
| Depth, D (m) | 19 | 1.9 | 0.601 |
| Design draught, T (m) | 10.8 | 1.08 | 0.342 |
| Length-depth ratio, $\frac{L_{PP}}{T}$ | 21.30 | 21.30 | 21.30 |
| Wetted surface area with a rudder, S (m^2) | 9539 | 95.39 | 9.553 |
| Displacement, FX (m3) | 52030 | 52.03 | 1.649 |
| Block coefficient, C_B | 0.6505 | 0.6505 | 0.6505 |
| Design speed, FX (m/s) | 12.3456 | 3.904 | 2.196 |
| Froude number at the design speed, F_n , FX | 0.26 | 0.26 | 0.26 |
| Speed range used in simulations, FX (m/s) | 6.17–13.37 | 1.95–4.23 | 1.10–2.38 |

simulations have the free surface and hence consider the wave-making behaviours such that the wave-making resistance is included in the total ship resistance (i.e. $R_T = R_F = R_{VP} + R_W$). The double-body simulations were modelled in three different scales (i.e. model-scale, moderate-scale, and full-scale) while the free-surface simulations were modelled only in the full-scales of the vessel. In order to examine the effect of different ship speeds, the simulations were conducted at Froude number ranges of 0.130–0.282 for KCS and 0.083–0.156 for KVLCC2, at

Table 3

Principal particulars and conditions of the KVLCC2 simulations, adapted from Kim et al. (2001) and Larsson et al. (2013).

| Main particulars | Full-scale | Moderate-scale | Model-scale |
|---|------------|----------------|-------------|
| Scale factor, λ | 1 | 10 | 58 |
| Length between the perpendiculars, FX (m) | 320 | 32 | 5.517 |
| Length of waterline, FX (m) | 325.5 | 32.55 | 5.612 |
| Beam at waterline, FX (m) | 58 | 5.8 | 1.000 |
| Depth, D (m) | 30 | 3 | 0.517 |
| Design draught, T (m) | 20.8 | 2.08 | 0.359 |
| Length-depth ratio, FX | 15.38 | 15.38 | 15.38 |
| Wetted surface area with a rudder, FX (m^2) | 27467.3 | 274.673 | 8.165 |
| Displacement, FX (m^3) | 312622 | 312.622 | 1.602 |
| Block coefficient, FX | 0.8098 | 0.8098 | 0.8098 |
| Design speed, V (m/s) | 7.9732 | 2.521 | 1.047 |
| Froude number at the design speed, F_n | 0.142 | 0.142 | 0.142 |
| Speed range used in simulations, V (m/s) | 4.63–8.74 | 0.86–1.62 | 0.61–1.14 |

each scale.

Fig. 4 illustrates the computational domain and the boundary conditions of the double-body and free-surface simulations of KCS and KVLCC2. In terms of the free-surface simulations, the velocity inlet and the pressure outlet boundary conditions were applied for the opposite faces in the longitudinal direction. The top and bottom far-field

boundaries were defined as velocity inlet. Symmetry boundary conditions were used for the vertical centre and side wall boundaries as similarly used by Terziev et al. (2019a). The surface boundary conditions of the hull and rudder were defined as no-slip walls. For the smooth surface condition, the smooth type wall-function was used, whereas the rough type roughness-functions, including the additional term of the roughness function were used for the fouling cases. The difference for the double-body simulations is that the $Z = 0$ plane is replaced with a symmetry plane such the simulation does not have the free surface. It is of note that all the simulations were conducted in fixed conditions (i.e. no sink or trim motions were allowed).

3.3. Mesh generation

Cut-cell grids with prism layer mesh on the walls were generated using the built-in meshing tool of STAR-CCM+ (version 13.06). Local refinements were made for finer grids in the critical regions, such as the bulbous bow, rudder, stern, and the region near the free surface (in case of the free-surface simulations), as shown in Fig. 5. The thickness of the first layer cell on the surface was chosen such that the wall y^+ values are higher than 30 and also higher than the k^+ values, as recommended by Demirel et al. (2017b), and Siemens (2018). It is of note that the same mesh was used for all the smooth and rough surface conditions, including the near-wall refinement. The mean wall y^+ values at the design speed on the wetted surface area of the model, moderate, and full-scale KCS simulations were 39, 63, and 205, respectively while, those for KVLCC2 simulations were 66, 52 and 93, respectively.

Table 4

Simulation cases.

| | | Double-body | Double-body | Double-body | Free-surface |
|--------------------|--------------------------|-------------------------------|-------------------------------|-------------------------------|-------------------------------|
| | | Full-scale | Moderate-scale | Model-scale | Full-scale |
| KCS | Scale factor, λ | 1 | 10 | 31.6 | 1 |
| | Speed range, V (m/s) | 6.17–13.37 | 1.95–4.23 | 1.10–2.38 | 6.17–13.37 |
| | F_n range | 0.13–0.282 | 0.13–0.282 | 0.13–0.282 | 0.13–0.282 |
| | Re_L range | $1.2\text{--}2.7 \times 10^9$ | $3.9\text{--}8.5 \times 10^7$ | $0.7\text{--}1.5 \times 10^7$ | $1.2\text{--}2.7 \times 10^9$ |
| KVLCC2 | Surface conditions | Smooth, S20%, M20%, B20% |
| | Scale factor, λ | 1 | 10 | 58 | 1 |
| | Speed range, V (m/s) | 4.63–8.74 | 0.86–1.62 | 0.61–1.14 | 4.63–8.74 |
| | F_n range | 0.083–0.156 | 0.083–0.156 | 0.083–0.156 | 0.083–0.156 |
| | Re_L range | $1.2\text{--}2.2 \times 10^9$ | $3.7\text{--}7.1 \times 10^7$ | $2.6\text{--}5.1 \times 10^6$ | $1.2\text{--}2.2 \times 10^9$ |
| Surface conditions | Smooth, S20%, M20%, B20% | Smooth, S20%, M20%, B20% | Smooth, S20%, M20%, B20% | Smooth, S20%, M20%, B20% | |

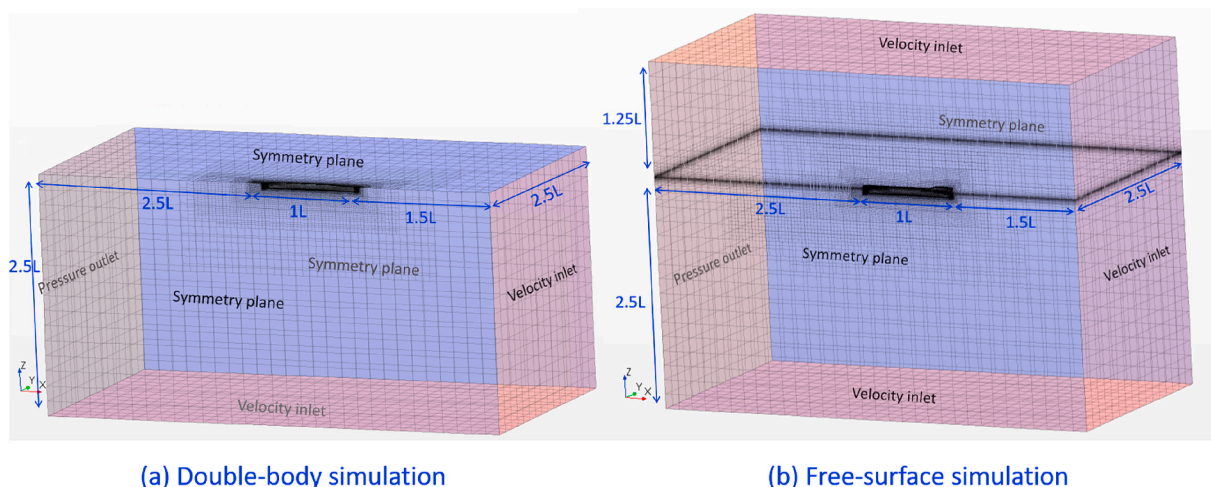


Fig. 4. Computational domain and the boundary conditions of KCS and KVLCC2 simulations.

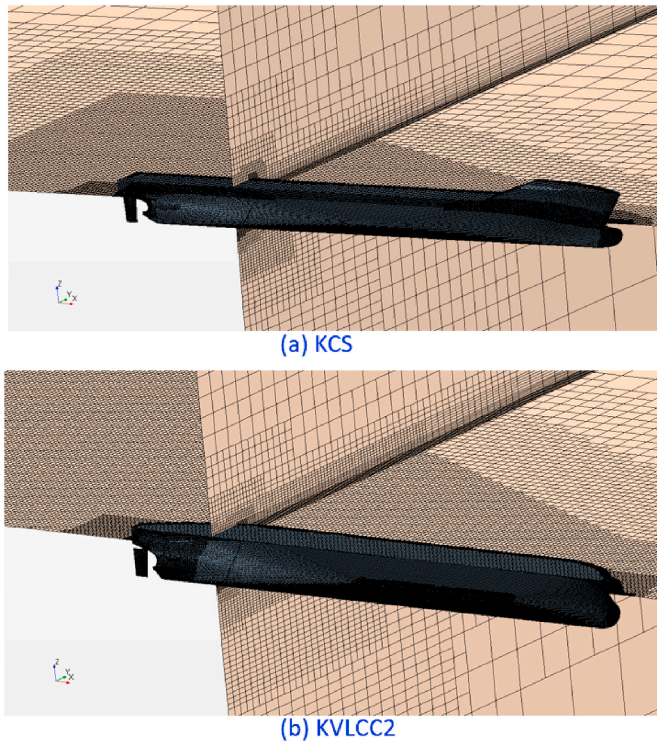


Fig. 5. Mesh structure of the computational domain of KCS and KVLCC2 simulations (free-surface models).

4. Results

4.1. Verification and validation

4.1.1. Verification study

In order to estimate the numerical uncertainties of the CFD models and also to determine the sufficient grid-spacings and the time-step size (Δt), a verification study was performed by conducting the simulations with three different resolutions of mesh and time steps, namely fine, medium and coarse. Then, the spatial and temporal uncertainties (U_{Grid} and $U_{\Delta t}$) were estimated using the Grid Convergence Index (GCI) method (Celik et al., 2008). It is of note that although the GCI method was firstly proposed for spatial convergence studies, it can also be used to estimate the temporal uncertainties of the simulations (Tezdogan et al., 2015; Terziev et al., 2018, 2019b, 2020).

Tables 5 and 6 show the spatial and temporal uncertainties of the KCS and KVLCC simulations, obtained from the grid and time-step convergence study. The spatial and temporal uncertainties were calculated based on the fine mesh and the fine time-step for each case. In this

study, the fine mesh and fine time step were used for each case.

4.1.2. Validation study

In order to validate the CFD models used in this study, the total resistance coefficients, C_T , obtained from the free-surface simulations were compared with C_T values of KCS and KVLCC2 at the design speed. Although the free-surface simulations with fouling conditions were modelled only at the full-scale, model-scale free-surface simulations were additionally conducted in this subsection to be compared against the model test of Kim et al. (2001). Full-scale C_T values were compared with other full-scale CFD studies available from the literature, as well as the extrapolated C_T values based on the experimental data of Kim et al. (2001). It is of note that the C_T of KCS was extrapolated using Froude's 2D scaling, while that of KVLCC2 was extrapolated using Hughes' 3D scaling, as per the suggestion of Dogrul et al. (2020).

The C_T values of KCS and KVLCC2 from the different sources and methods are shown in Tables 7 and 8, respectively. The relative differences were calculated using the current CFD results as the reference values. The model-scale results for KCS and KVLCC2 showed good agreement with the experimental data of Kim et al. (2001), showing the relative differences of 0.35% and -1.59% , respectively. In terms of full-scale simulations, both the KCS and KVLCC2 results from the present CFD showed good agreement with other full-scale CFD results in the literature showing relative differences (up to -1.25%). However, the current KVLCC2 simulation showed a rather large difference with the extrapolated result (-4.69%), as similarly observed by Dogrul et al. (2020) and Farkas et al. (2020b).

4.2. Roughness effect on C_F and C_V

In order to investigate the roughness effect on the frictional resistance, C_F , and viscous resistance, C_V , the double-body simulations of KCS and KVLCC2 were performed. As mentioned earlier, the total resistance of the vessels calculated in the double-body simulations is assumed to be equal to the viscous resistance (i.e. $C_T = C_V$), while C_F is calculated by simply considering the shear drag only in the simulations.

Figs. 6 and 7 show the C_F and C_V values obtained from the KCS and KVLCC2 simulations, respectively, in different surface conditions (Smooth, S20%, M20% and B20%). As shown in the figures, the C_F and C_V values increase significantly due to the hull fouling. For the KCS cases, the percentage increase in the frictional resistance, $\% \Delta C_F$, with the most severe fouling condition (B20%) are up to 93%, 89%, and 86%, at the model, moderate, and full-scales, respectively. And those of KVLCC2 are 79%, 74%, and 69%. One can notice that the $\% \Delta C_F$ values are larger for KCS than KVLCC2, while these values become smaller as the ship length increases. This can be explained by two factors; the relative roughness height, k/L , and the roughness Reynolds number, $k^+ = kU_\tau/\nu$, where, k , U_τ and ν are the roughness height, friction velocity, and the kinematic viscosity, respectively. It is a well-known fact

Table 5
Spatial and temporal convergence study of the KCS simulations.

| | | Double-body | | Double-body | | Double-body | | Free-surface | |
|-----------------------|--------|------------------------------|-----------|-----------------------------------|-----------|----------------------------------|-----------|------------------------------|------------|
| | | Full-scale ($\lambda = 1$) | | Moderate-scale ($\lambda = 10$) | | Model-scale ($\lambda = 31.6$) | | Full-scale ($\lambda = 1$) | |
| | | No.Cells | R_V (N) | No.Cells | R_V (N) | No.Cells | R_V (N) | No.Cells | R_T (N) |
| Spatial convergence | Coarse | 524,829 | 591,515 | 435,628 | 878.15 | 229,144 | 36.083 | 1,005,230 | 768,434.74 |
| | Medium | 695,031 | 581,901 | 596,259 | 875.50 | 316,815 | 35.978 | 1,407,062 | 767,334.76 |
| | Fine | 963,216 | 578,655 | 815,837 | 870.96 | 479,982 | 35.954 | 2,019,668 | 765,293.29 |
| U_{Grid} (Fine) | | | 0.246% | | 0.909% | | 0.013% | | 0.481% |
| Temporal convergence | | Δt (s) | R_V (N) | Δt (s) | R_V (N) | Δt (s) | R_V (N) | Δt (s) | R_T (N) |
| | Coarse | 0.04 | 577,156 | 0.04 | 870.55 | 0.04 | 35.947 | 0.04 | 766,944.79 |
| | Medium | 0.02 | 577,717 | 0.02 | 870.66 | 0.02 | 35.948 | 0.02 | 765,097.03 |
| | Fine | 0.01 | 578,655 | 0.01 | 870.96 | 0.01 | 35.954 | 0.01 | 765,293.29 |
| $U_{\Delta t}$ (Fine) | | | 0.302% | | 0.023% | | 0.005% | | 0.036% |
| U_{total} | | | 0.389% | | 0.909% | | 0.014% | | 0.483% |

Table 6
Spatial and temporal convergence study of KVLCC2 simulations.

| | | Double-body | | Double-body | | Double-body | | Free-surface | |
|-----------------------|----------------|------------------------------|-----------|-----------------------------------|-----------|----------------------------------|-----------|------------------------------|------------|
| | | Full-scale ($\lambda = 1$) | | Moderate-scale ($\lambda = 10$) | | Model-scale ($\lambda = 31.6$) | | Full-scale ($\lambda = 1$) | |
| Spatial convergence | No.Cells | | R_V (N) | No.Cells | R_V (N) | No.Cells | R_V (N) | No.Cells | R_T (N) |
| | Coarse | 712,288 | 782,485 | 598,405 | 1,192.16 | 578,599 | 9.289 | 1,525,249 | 803,512.69 |
| | Medium | 1,068,217 | 775,411 | 917,246 | 1,189.64 | 800,617 | 9.269 | 2,267,933 | 800,629.00 |
| U_{Grid} (Fine) | Fine | 1,571,155 | 772,577 | 1,371,184 | 1,188.14 | 1,104,198 | 9.259 | 3,543,146 | 788,229.32 |
| | | | 0.347% | | 0.283% | | 0.149% | | 0.781% |
| Temporal convergence | Δt (s) | | R_V (N) | Δt (s) | R_V (N) | Δt (s) | R_V (N) | Δt (s) | R_T (N) |
| | Coarse | 0.08 | 771,365 | 0.08 | 1,188.23 | 0.04 | 9.259 | 0.08 | 801,500.37 |
| | Medium | 0.04 | 771,774 | 0.04 | 1,188.09 | 0.02 | 9.258 | 0.04 | 788,930.44 |
| $U_{\Delta t}$ (Fine) | Fine | 0.02 | 772,577 | 0.02 | 1,188.14 | 0.01 | 9.259 | 0.02 | 788,446.66 |
| | | | 0.135% | | 0.003% | | 0.001% | | 0.003% |
| U_{total} | | | 0.373% | | 0.283% | | 0.149% | | 0.781% |

Table 7
values of KCS obtained from present CFD and other sources and methods. $F_n = 0.26$

| Ship | Source or method | C_T | Relative difference |
|-------------|---|-----------|---------------------|
| Model-scale | Present CFD | 3.544E-03 | |
| | EFD of Kim et al. (2001) | 3.556E-03 | 0.35% |
| Full-scale | Present CFD | 2.107E-03 | |
| | CFD of Dogrul et al. (2020) | 2.113E-03 | 0.26% |
| | CFD of Farkas et al. (2020b) | 2.081E-03 | -1.25% |
| | CFD of Demirel et al. (2017) | 2.097E-03 | -0.49% |
| | Extrapolation based on EFD of Kim et al. (2001) | 2.084E-3 | -1.13% |

Table 8
values of KVLCC2 obtained from present CFD and other sources and methods. $F_n = 0.142$

| Ship | Source or method | C_T | Relative difference |
|-------------|---|-----------|---------------------|
| Model-scale | Present CFD | 4.176E-03 | |
| | EFD of Kim et al. (2001) | 4.110E-03 | -1.59% |
| Full-scale | Present CFD | 1.806E-03 | |
| | CFD of Dogrul et al. (2020) | 1.806E-03 | -0.03% |
| | CFD of Farkas et al. (2020b) | 1.795E-03 | -0.63% |
| | Extrapolation based on EFD of Kim et al. (2001) | 1.722E-03 | -4.69% |

that the skin friction over a rough wall increases with the k/L values (Moody, 1944; Demirel et al., 2019). Therefore, even with the same fouling condition, the roughness effect on C_F is stronger for smaller vessels due to the larger k/L ratios.

On the other hand, considering the significant changes in ship lengths, the changes in $\% \Delta C_F$ with the scale is relatively small. For example, while the ship length of KVLCC2 increases 58 times (i.e. the k/L ratio becomes 58 times smaller), the $\% \Delta C_F$ reduces by 10% only. This can be attributed to the fact that the k^+ values increase due to the increasing ship speeds with the scale at the same F_n . Therefore, higher k^+ values result in stronger roughness effects in the turbulent boundary layer, which diminishes the decreasing trends of $\% \Delta C_F$ due to the rapid changes in the k/L ratio. Fig. 8 compares the k^+ values on the hull of KCS

and KVLCC2 at their design speed (constant F_n) with the B20% fouling condition. The k^+ values appear to be higher with larger scales and also higher for KCS due to the higher speeds.

When it comes to the viscous resistance, C_V , similar trends were observed. For the KCS cases, the percentage increase in the viscous resistance, $\% \Delta C_V$, due to the most severe fouling condition (B20%) are up to 88%, 87%, and 84%, at the model, moderate, and full-scales, respectively. And those of KVLCC2 are 78%, 74%, and 71%. It can also be found that the differences between C_V and C_F are larger for KVLCC2 than KCS (including the smooth surface condition), which signifies larger viscous pressure resistance, C_{VP} , and hence larger form factor values, $1+k$.

4.3. Roughness effect on form factor $1+k$

Fig. 9 compares the form factors, $1+k$, of KCS and KVLCC2 with the different surface conditions. The $1+k$ values were calculated using the C_F and C_V values obtained from the double-body simulations, as $1+k = C_V/C_F$. As shown in the figure, the roughness effect of barnacles on the $1+k$ values showed different trends for KCS and KVLCC2. For the KCS cases, the $1+k$ values decrease due to hull fouling and these decreases become more significant as the hull size increases. The reduction in the form factor implies that the increase due to hull fouling is more significant for C_F than C_{VP} .

On the other hand, differences were found in the KVLCC2 cases, although the roughness effect on the $1+k$ values of KVLCC2 showed a different trend at each scale. In the model-scale ($\lambda = 58$), the $1+k$ values increase with the presence of hull fouling. The roughness effect on $1+k$ become minor at the moderate-scale ($\lambda = 10$) and finally the $1+k$ values decrease at the full-scale ($\lambda = 58$). These different trends indicate that the roughness effect of C_{VP} is more significant than that of C_F at small scales but the effect of C_F becomes dominant as the hull size increases, which agrees with the KCS cases.

These differences in the roughness effect on the form factors can be more clearly seen in Fig. 10 which compares the percentage increase in the frictional and viscous pressure resistance components, $\% \Delta C_F$ and $\% \Delta C_{VP}$. The $y = x$ line was drawn together for comparison, which indicates that $\% \Delta C_F$ and $\% \Delta C_{VP}$ are equal along the line. For KCS, the results shown in Fig. 10 are located under the $y = x$ line, which means that the roughness effect of C_F dominates to that of C_{VP} and the results move to the right-bottom side as the scale increases suggesting that this dominance becomes stronger with larger hull sizes. When it comes to the KVLCC2 case, the results for the model-scale ($\lambda = 58$) simulation are found above the $y = x$ line, showing the dominance of the roughness effect of C_{VP} over C_F , but move to the right-bottom side of the graph as the scale increases, similarly to the KCS case. The general trend in these differences can be summarised that as the scale increases, the roughness effect of C_F becomes more important than that of C_{VP} for both the vessels.

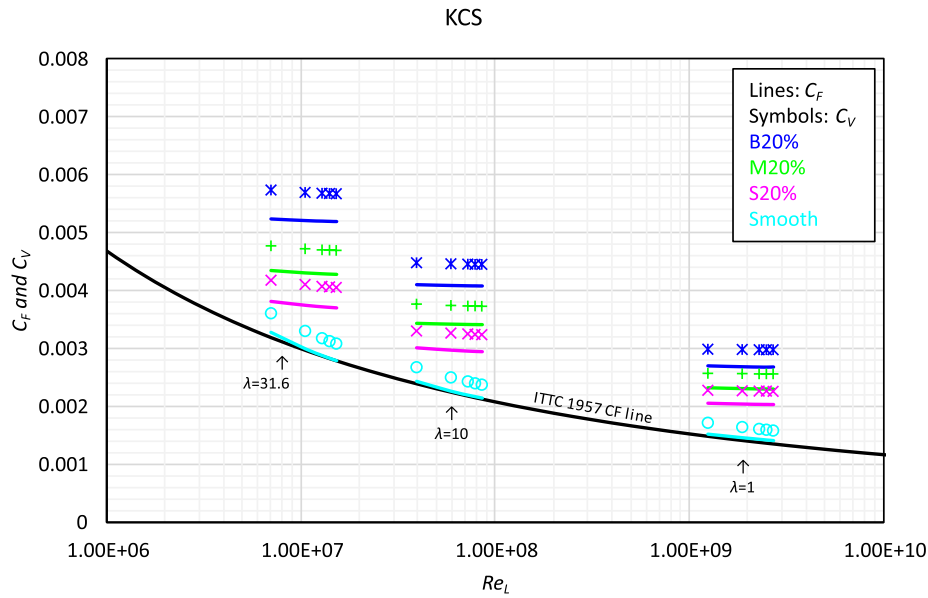


Fig. 6. C_F and C_V of KCS with different hull conditions at model ($\lambda = 31.6$), moderate ($\lambda = 10$) and full-scale ($\lambda = 1$).

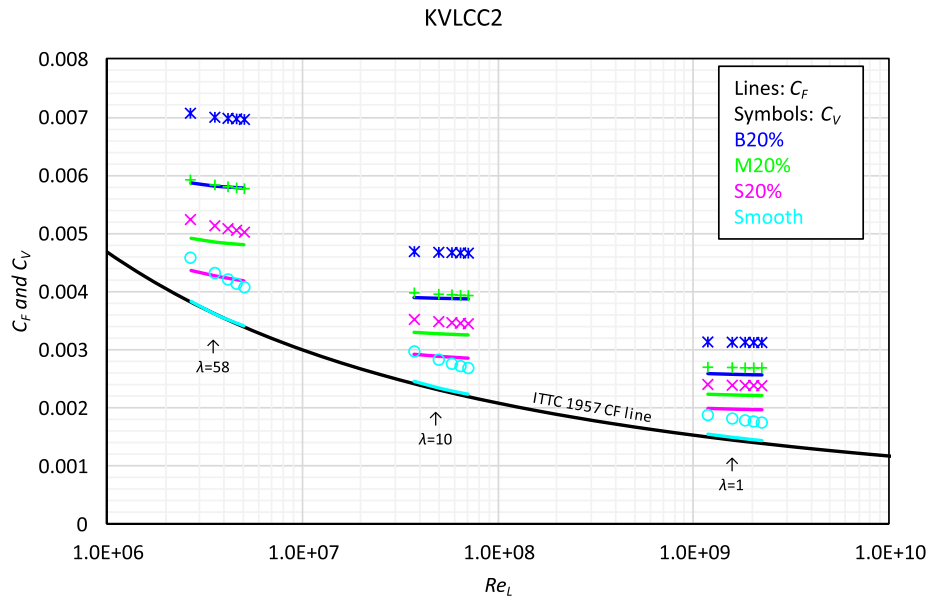


Fig. 7. C_F and C_V of KVLCC2 with different hull conditions at model ($\lambda = 58$), moderate ($\lambda = 10$) and full-scale ($\lambda = 1$).

4.4. Free-surface simulations

4.4.1. Roughness effect on C_T

In order to investigate the roughness effect on the total resistance, C_T , full-scale free-surface simulations of KCS and KVLCC2 were conducted with varying speeds for the smooth and fouling (S20%, M20%, B20%) surface conditions. Figs. 11 and 12 show the C_T values of KCS and KVLCC2, respectively, with and without the presence of hull fouling. Significant increases in C_T were recorded for both the ships. The percentage increases, $\% \Delta C_T$ due to the most severe fouling condition (B20%) for KCS and KVLCC2 were up to 66% and 78%, respectively. It is interesting to note that the KVLCC2 case shows higher $\% \Delta C_T$ values although they have smaller $\% \Delta C_F$ as shown in section 4.2. This can be explained by the fact that KVLCC2 has a higher contribution of the frictional resistance in the total resistance than KCS due to slower speed (lower Fn).

Another interesting feature is to note that the $\% \Delta C_T$ values of KCS

show a decreasing trend with the ship speed while those of KVLCC2 show the opposite. In order to find the rationale behind these differences, the total resistance components were divided into different components and discussed in the following sections.

4.4.2. Roughness effect on C_F and C_R

The total resistance coefficients, C_T , were decomposed into the frictional resistance coefficients, C_F , and the residuary resistance coefficients, C_R , by simply dividing the total drag acting on the ship into the shear and pressure force components. Figs. 13 and 14 show the C_F and C_R values of the full-scale KCS and KVLCC2 models, respectively, in the smooth and fouled (S20%, M20%, B20%) hull conditions. It is of note that the C_F values in Figs. 13 and 14 are from the free-surface simulations and these values can be slightly different ($\sim 1\%$) from the C_F values of the double-body simulations (Figs. 6 and 7) mainly because of the changes in the wetted surface area due to free surface elevations.

Both the KCS and KVLCC2 simulations showed significant increases

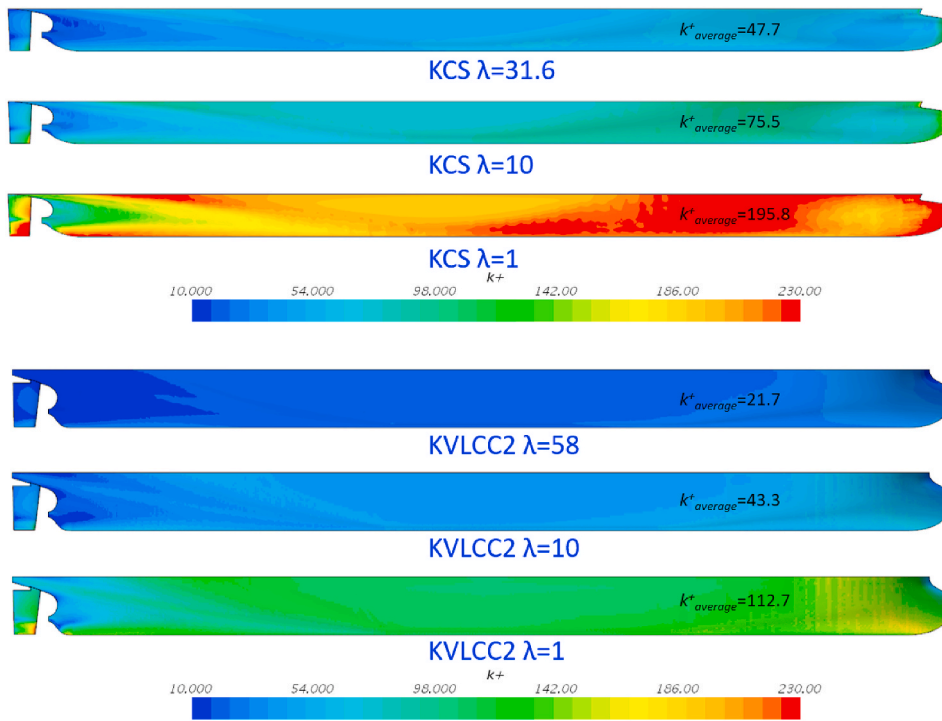


Fig. 8. k^+ on the hulls of KCS and KVLCC2 with B20% fouling condition.

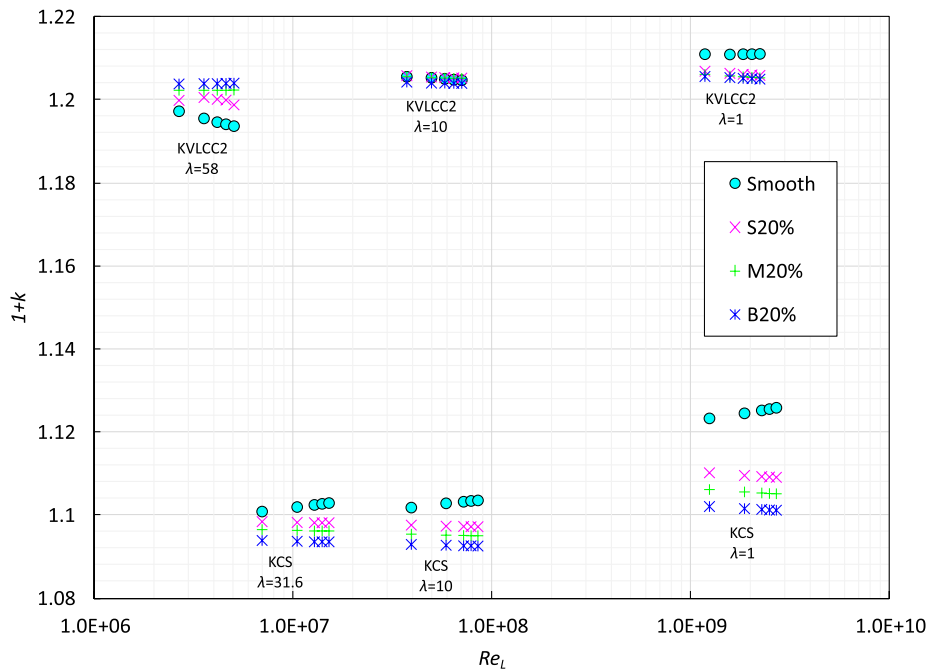


Fig. 9. of KCS and KVLCC2 for different surface conditions.

in C_F due to the hull fouling as already observed in Figs. 6 and 7, while some differences were observed on C_R of KCS and KVLCC2. The C_R values of KVLCC2 show significant increases due to the hull fouling and these increases are consistent with the varying speeds. On the other hand, the C_R values of KCS showed relatively small increases with hull fouling at low speed. These increases become smaller as the speed increases and eventually turn into decreases at higher speeds. Together with this feature, the increasing dominance of C_R in C_T for the KCS case can be related to the decreasing $\% \Delta C_T$ values of KCS as the speed increases as shown in Fig. 11.

In order to understand the rationale of the changing trends of the roughness effect on C_R , the residuary resistance values were further decomposed into the viscous pressure resistance, C_{VP} , and the wave-making resistance, C_W and discussed in the following section.

4.4.3. Roughness effect on C_{VP} and C_W

The C_R values were decomposed into C_{VP} and C_W using the form factor values obtained from the double-body simulations as

$$C_{VP} = kC_F \tag{11}$$

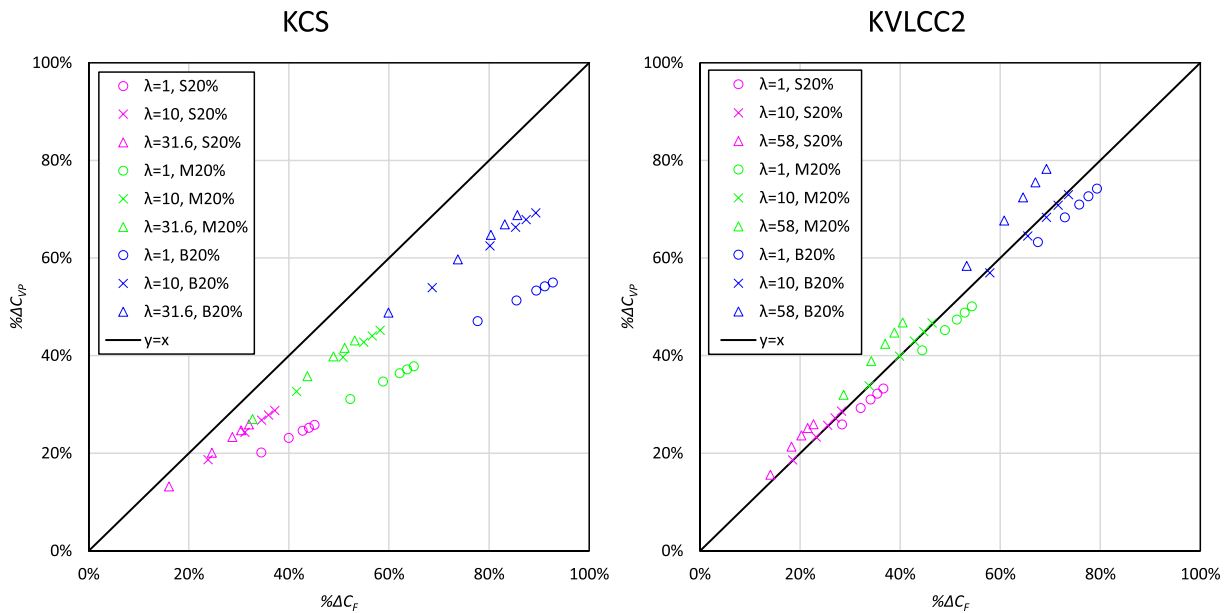


Fig. 10. vs $\% \Delta C_{VP}$ due to the fouling conditions of KCS (left) and KVLCC2 (right).

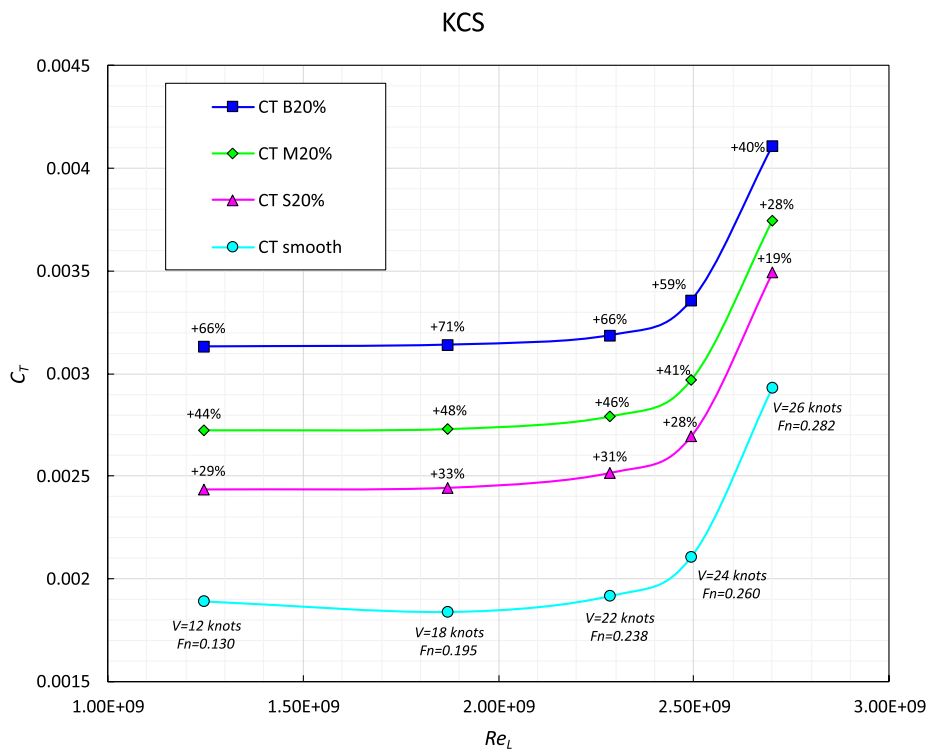


Fig. 11. of KCS with different hull conditions.

$$C_W = C_R - C_{VP} \tag{12}$$

Figs. 15 and 16 show the C_{VP} and C_W values of KCS and KVLCC2, respectively, with the smooth (S20%, M20%, B20%) hull conditions. In terms of C_{VP} , both the KCS and KVLCC2 cases show significant increases due to the hull fouling (up to 52% and 74% for KCS and KVLCC2 respectively). On the other hand, differences were also found on C_W between the two hull types.

For the KCS case, the C_W values have relatively high contributions in C_R and increase sharply as the speed increases and eventually become dominant over C_{VP} . The roughness effect on the C_W values of KCS is

negligible at the lowest speed but becomes more pronounced as the ship speed increases (which can be related to the higher k^+ values at higher speeds). The C_W values of KCS show decreases due to hull fouling. And the magnitudes of decrease become larger as the dominance of C_W increases. Consequently, for the fouled KCS cases, the decreases in C_W cancel the increases in C_{VP} and eventually the C_R values start to decrease at higher speeds.

On the other hand, the C_W values of KVLCC2 have minor contributions and remain rather consistent with the speed. Accordingly, for KVLCC2, the roughness effect on C_R follows the trend of C_{VP} . It is interesting that at the high speeds, the roughness effect causes increases

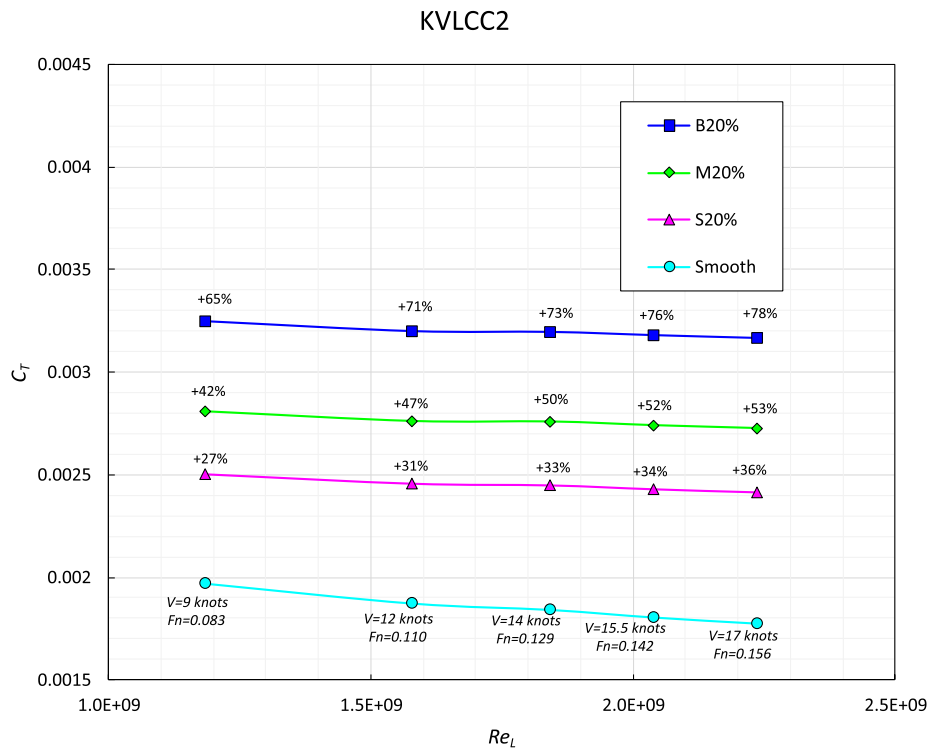


Fig. 12. of KVLCC2 with different hull conditions.

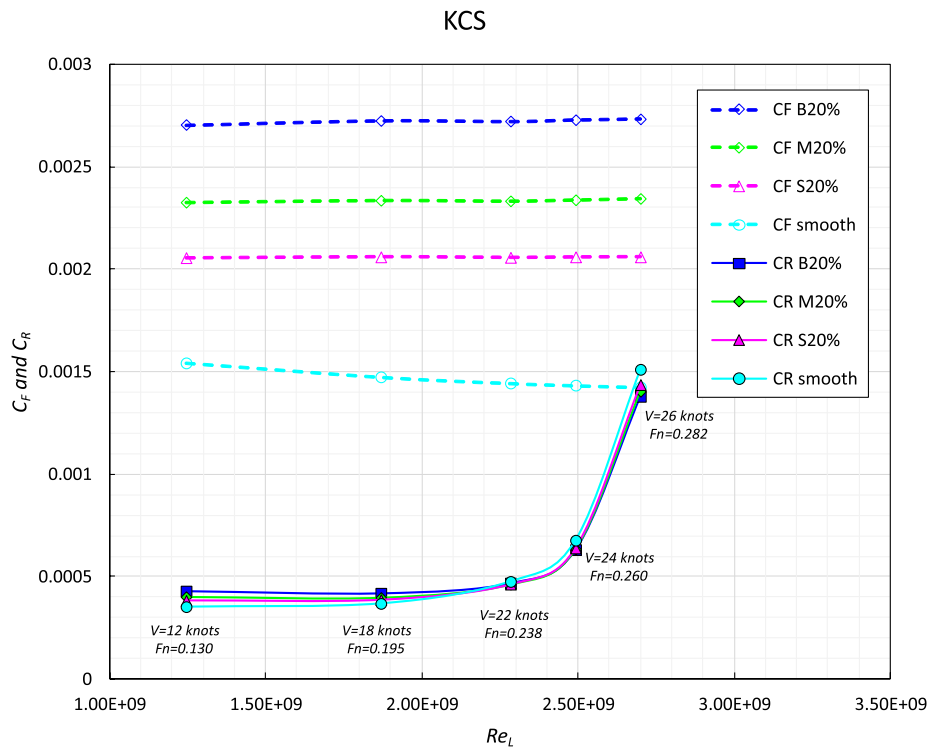


Fig. 13. of KCS with different hull conditions.

in C_W unlike the KCS case. However, these changes in C_W are too small (i.e. $\Delta C_W / C_T < 0.5\%$) to draw any reliable conclusion on their effects, considering that the estimated numerical uncertainty of C_T of the free-surface KVLCC2 simulation is larger than these changes ($U_{total} = 0.78\%$). It is of note that the numerical uncertainty of the C_W

values ($U_{C_W} = \sqrt{\left(\frac{\partial C_W}{\partial C_T} U_{C_T}\right)^2 + \left(\frac{\partial C_W}{\partial C_V} U_{C_V}\right)^2} = \sqrt{U_{C_T}^2 + U_{C_V}^2}$), for the KCS and KVLCC2 simulations at the design speeds are 2.36% and 54.6%, respectively.

This observation suggests that the roughness effect on the wave-

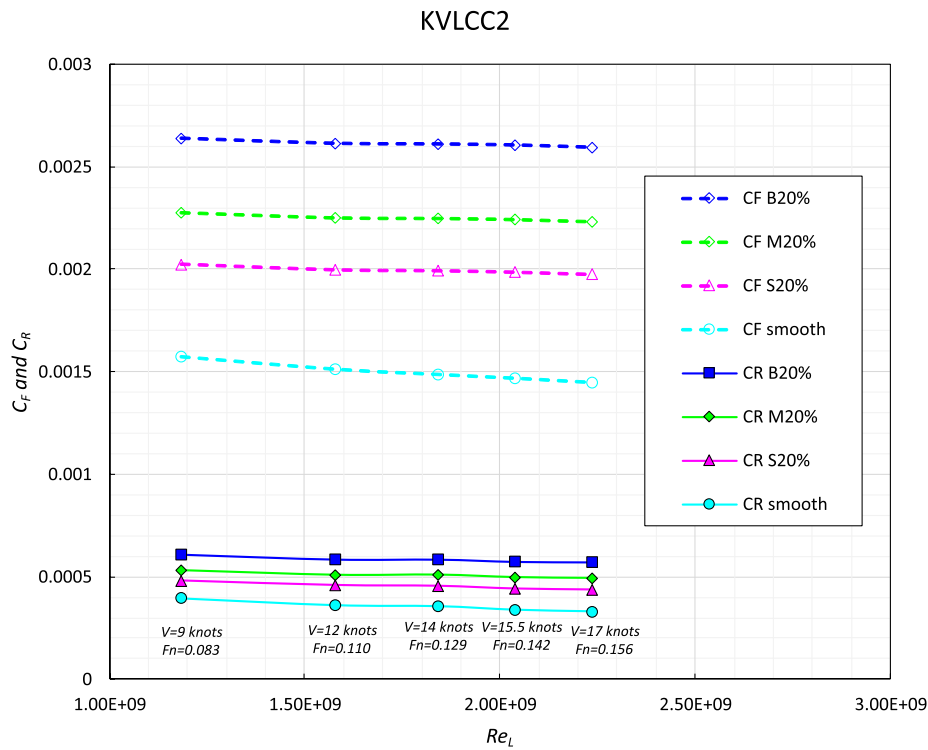


Fig. 14. of KVLCC2 with different hull conditions.

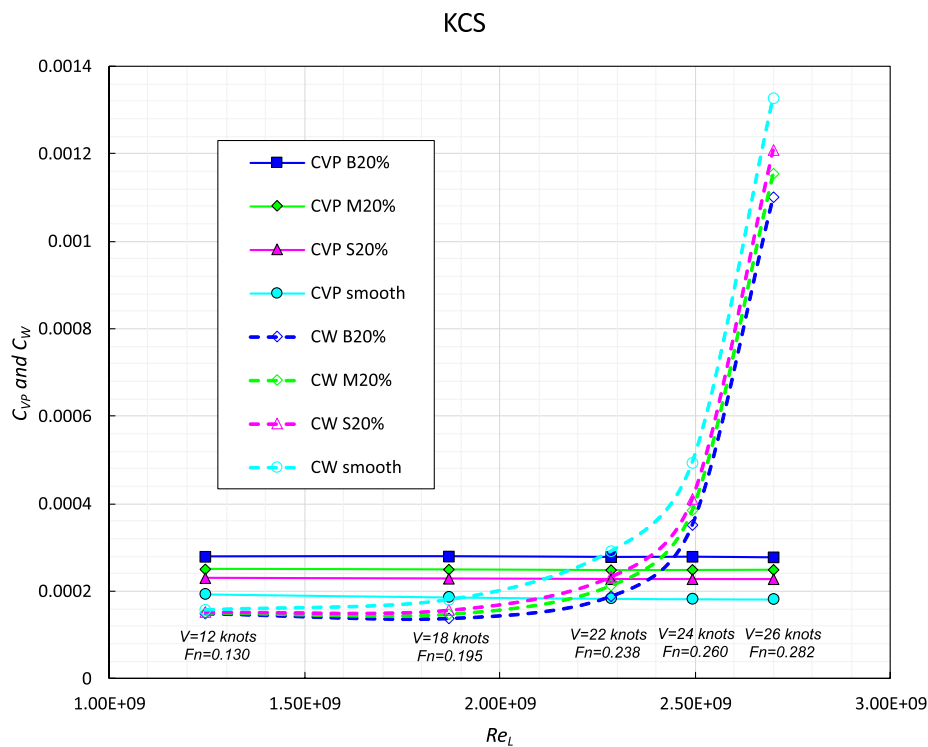


Fig. 15. and C_w of KCS with different hull conditions.

making resistance can differ by the hull forms and also by the speed. These differences can be correlated with many different factors (e.g. the block coefficient, and the Froude number, Fn). Further investigations with sufficient variations are required to understand better the correlations between these factors and the roughness effect on C_w

4.5. Roughness effect on the flow field

4.5.1. Velocity field

Figs. 17 and 18 show the axial velocity contours around the KCS and KVLCC2 hulls, respectively, in different scales with the smooth surface conditions and the most severe fouling conditions (B20%). The mean

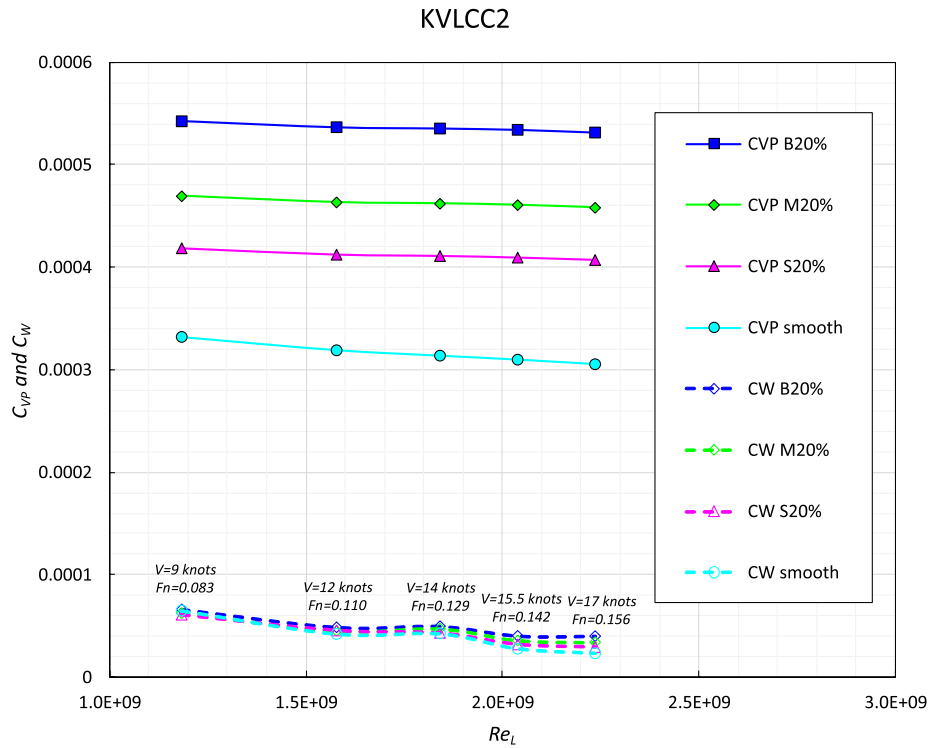


Fig. 16. and C_w of KVLCC2 with different hull conditions.

axial velocity was normalised by dividing the velocity with the advance speed of the ship (V_x/V_{ship}). As shown in the figures, for both the hull forms at the respective scales, the roughness effect brings significant changes in the velocity field around the hulls. As expected, the smaller sizes with fouling showed larger wake regions due to the decelerated flow velocity at the stern. The roughness effect on the wake field can be more clearly seen in Fig. 19, which compares the axial velocity contours behind the hull on the propeller plane ($x = 0.0175L_{pp}$).

In order to quantify the increases in the stern wake, the nominal wake fractions, w_n , were calculated by surface averaging the local wake fraction, $w'_x = (V_{ship} - V_x)/V_{ship}$, on the propeller disc (i.e. the disc where the propeller will be located). Figs. 20 and 21 compare the w_n of the KCS and KVLCC2, respectively, with the smooth and most severe fouling conditions (B20%). The inner and outer circles represent the hub diameter and propeller diameter. For both the hull forms, the hull fouling resulted in significant increases in the w_n values. The percentage increases in the w_n of KCS due to the hull fouling at the model, moderate and the full-scale are 53%, 54%, and 45%, while those for the KVLCC2 case are 35%, 43%, and 43%.

4.5.2. Boundary layer thickness

Another notable feature of the fouling effect is observed in Figs. 17 and 18 is the increase in the boundary layer thickness, especially on the hull bottom as well as on the aft end region. The increases in the boundary layer thicknesses can be seen more clearly in Figs. 22 and 23 where the boundary layers are represented by the axial velocity contours limited to $V_x/V_{ship} = 0.9$. The figures vividly show the growth in the boundary layer thickness due to the hull fouling (B20%) for both the ships at all the scales. These arguments in the boundary layer thickness that can be related to the presence of hull fouling reflect on to the frictional and viscous pressure resistance as discussed earlier.

4.5.3. Pressure field

Figs. 24 and 25 illustrate the surface pressure distribution on the stern region of KCS and KVLCC2, respectively, in both the smooth and fouled (B20%) conditions. The pressure was normalised by dividing it by the dynamic pressure ($1/2\rho V_{ship}^2$). For both the ship types in all the scales, reduced pressure magnitudes at the stern were observed with the presence of surface fouling, i.e. reduced pressure recovery. Correspondingly, the decreased stern pressures bring increased viscous

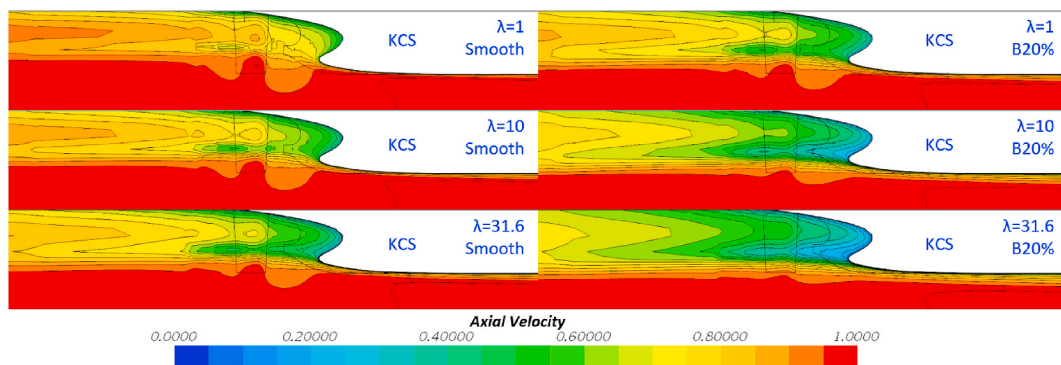


Fig. 17. Axial velocity (V_x/V_{ship}) around KCS hulls in different scales with smooth and B20% surface conditions (on $y = 0.006L_{pp}$ plane)

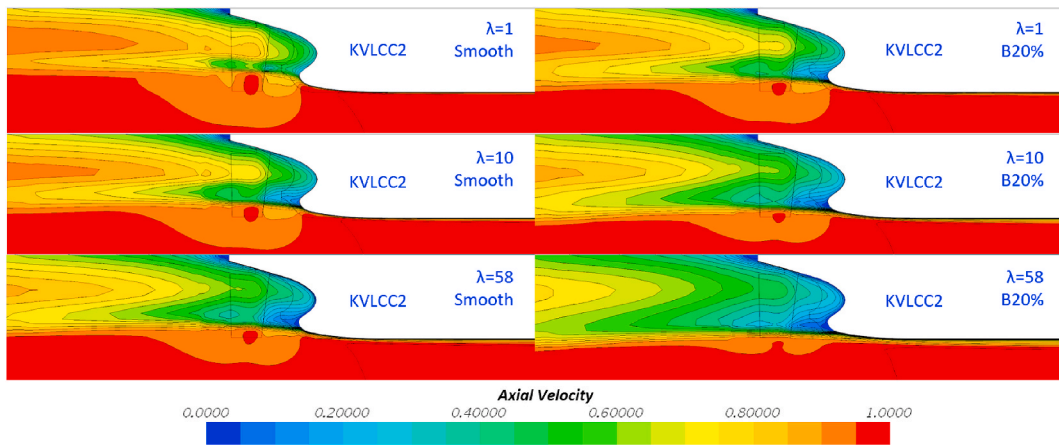


Fig. 18. Axial velocity (V_x/V_{ship}) around KVLCC2 hulls in different scales with smooth and B20% surface conditions (on $y = 0.006L_{pp}$ plane)

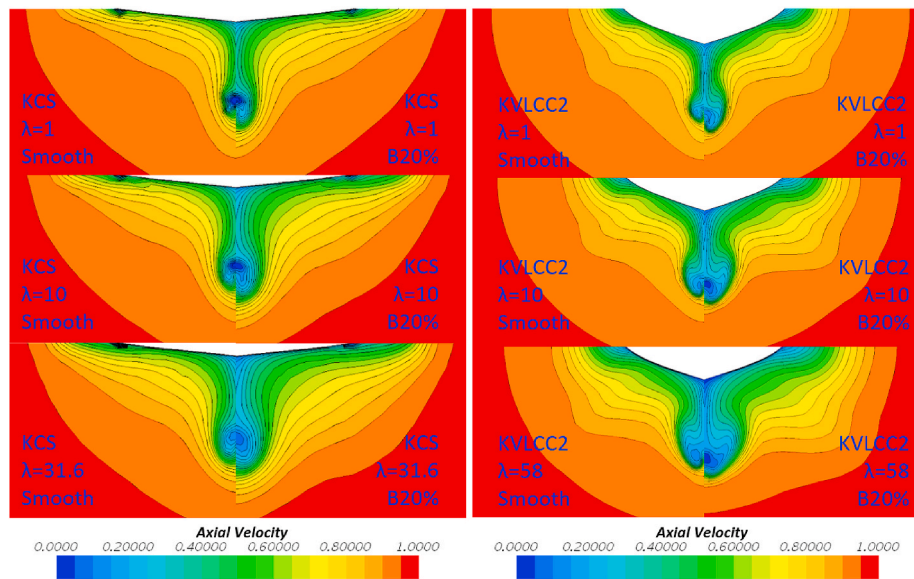


Fig. 19. Axial velocity (V_x/V_{ship}) behind KCS (left) and KVLCC2 (right) in different scales with smooth and B20% surface conditions (on $x = 0.0175L_{pp}$ plane).

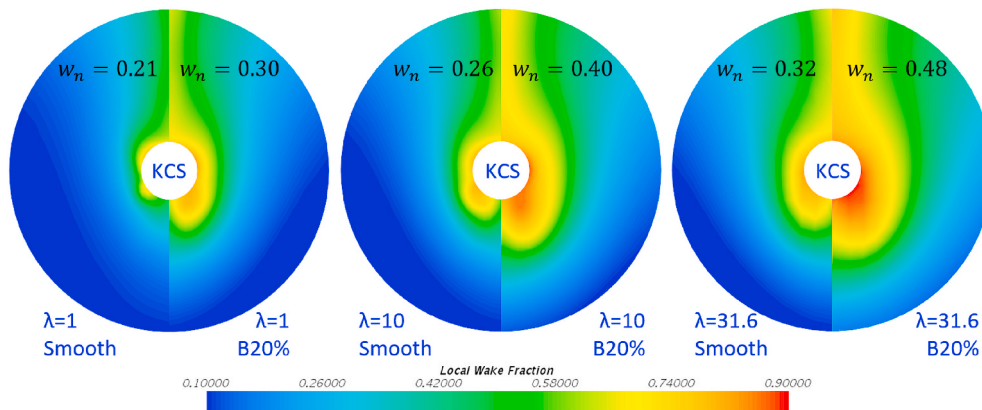


Fig. 20. Local wake fraction, w_n , at the propeller plane of KCS in different scales with smooth and B20% surface conditions.

pressure resistances, as shown in Figs. 15 and 16.

4.5.4. Wave elevation

Fig. 26 compares the Kelvin wave around the KCS hull with and

without the surface fouling at low and high speeds. While considerable differences were observed between the smooth and fouled (B20%) hulls at the high speed ($Fn = 0.282$), almost no effects were noted at the low speed ($Fn = 0.13$). These speed dependent effects of the roughness on

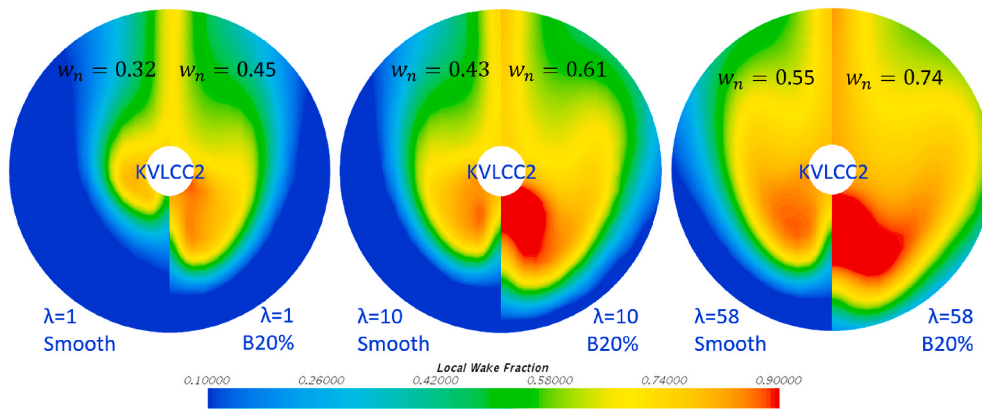


Fig. 21. Local wake fraction, w_x' , at the propeller plane of KVLCC2 in different scales with smooth and B20% surface conditions.

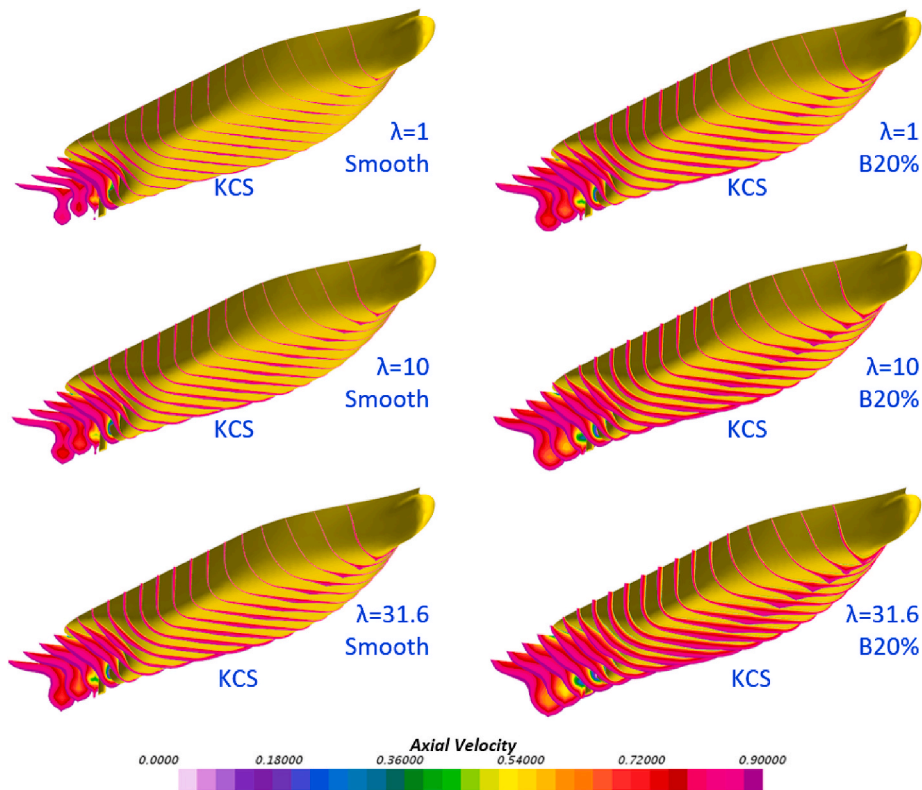


Fig. 22. Boundary layer represented by slices limited to axial velocity ($V_x/V_{ship} = 0.9$) around KCS hulls in different scales with smooth and B20% surface conditions.

the wave elevations are in agreement with those on the wave-making resistance, C_w , of KCS as shown in Fig. 16, where the effect was negligible at the low speed whereas the effect becomes substantial as the speed increases.

Likewise, as shown in Fig. 27, the roughness effect on the Kelvin wave around the KVLCC2 showed correspondences with the roughness effect on the C_w values, also shown in Fig. 17. For both the low and high speeds, the free surface elevations around the KVLCC2 hull showed almost no differences regardless of the presence of hull fouling.

4.5.5. Concluding remarks

In the study presented here, URANS based CFD simulation models of two different types of hulls and sizes were developed to investigate the effect of the ship type and scales on the resistances of these ships in the presence of fouling. The CFD simulations were performed using the benchmark ship hulls of a container ship (KCS) and a tanker (KVLCC2).

For the representation of the roughness effect due to hull fouling, the modified wall-function approach was used with the roughness function of barnacles.

Spatial and temporal convergence studies were performed using the Grid convergence Index (GCI) method, to estimate the numerical uncertainties of the proposed CFD models and to determine sufficient grid-spacings and time steps.

By using two different computational domain types (i.e. double-body and free-surface) the ship resistance was decomposed into its individual components. The results showed that the hull fouling causes significant increases in the frictional resistance and the viscous resistance regardless of the hull forms and scales (i.e. sizes). On the other hand, while the form factors of KVLCC2 showed a different trend at each scale, those of KCS consistently showed decreases with hull fouling. Differences between the effects of the hull types were also found through the roughness effect on the wave-making resistance. Whereas the wave-making

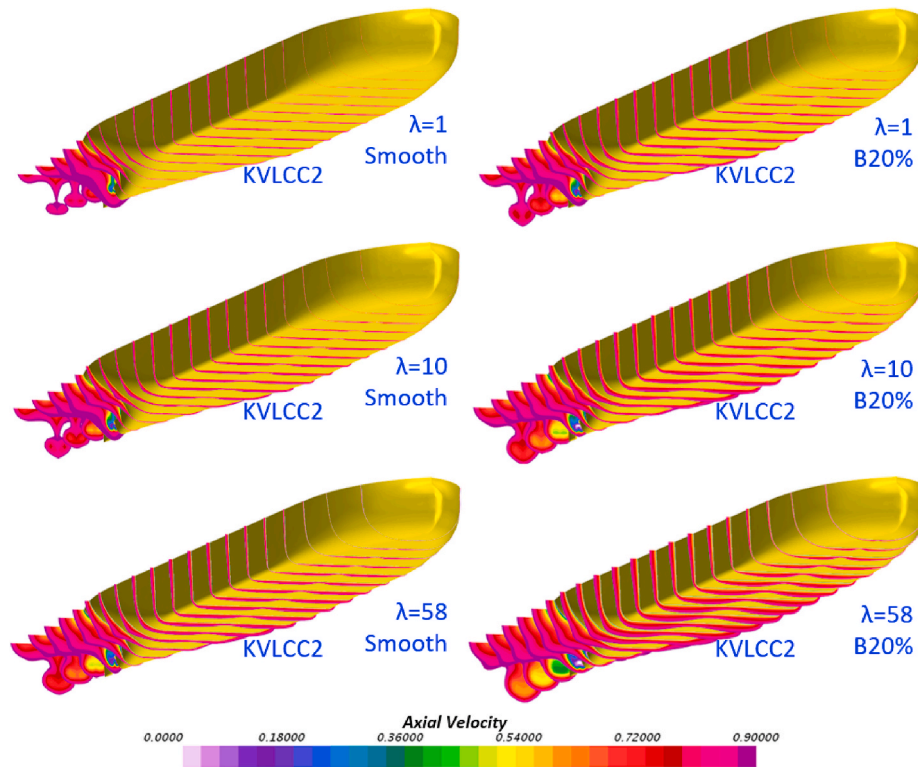


Fig. 23. Boundary layer represented by slices limited to axial velocity ($V_x/V_{ship} = 0.9$) around KVLCC2 hulls in different scales with smooth and B20% surface conditions.

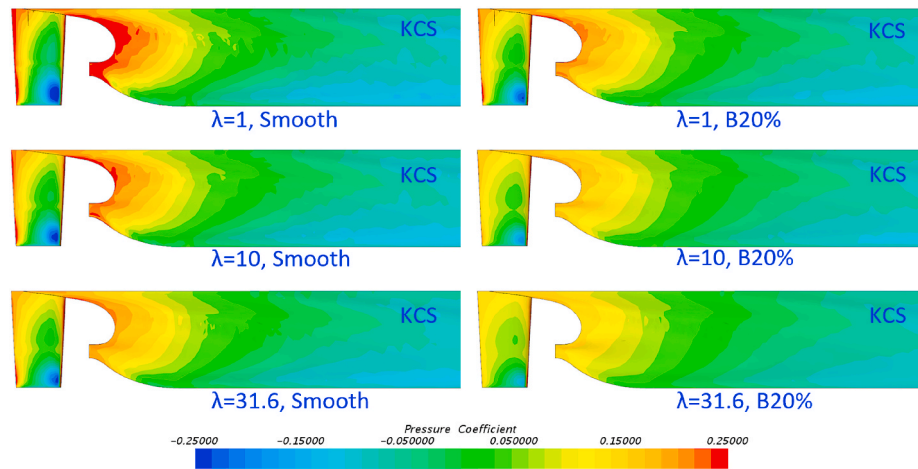


Fig. 24. Pressure coefficient on stern region of KCS in different scales with smooth and B20% surface conditions.

resistance of KVLCC2 showed almost no differences regardless of the presence of the hull fouling, KCS showed considerable roughness effects on the wave-making resistance at the high speed. In contrast, this effect was negligible at the low speed of KCS. Finally, the effect of hull fouling on the flow characteristics around the hulls was examined that included the velocity field downstream of the hulls and nominal wake flow at the propeller planes, boundary layer thickness and pressure distribution on the hulls and the Kelvin wave patterns.

The study provided several important findings including the first investigation into the different features of roughness effect for different hull forms, ship size and speeds. However, to establish a more comprehensive understanding of the correlations of the roughness effect with various factors such as block coefficient, Froude number, etc., the study should be further extended with sufficient variations of hull forms,

scales and speeds.

CRedit authorship contribution statement

Soonseok Song: Writing - original draft, Formal analysis, Investigation, Validation, Visualization, Data curation. **Yigit Kemal Demirel:** Conceptualization, Methodology, Supervision, Writing - review & editing, Project administration, Resources, Funding acquisition, Supervision. **Claire De Marco Muscat-Fenech:** Writing - review & editing, Project administration, Funding acquisition. **Tahsin Tezdogan:** Writing - review & editing, Project administration, Supervision. **Mehmet Atlar:** Writing - review & editing, Project administration, Supervision.

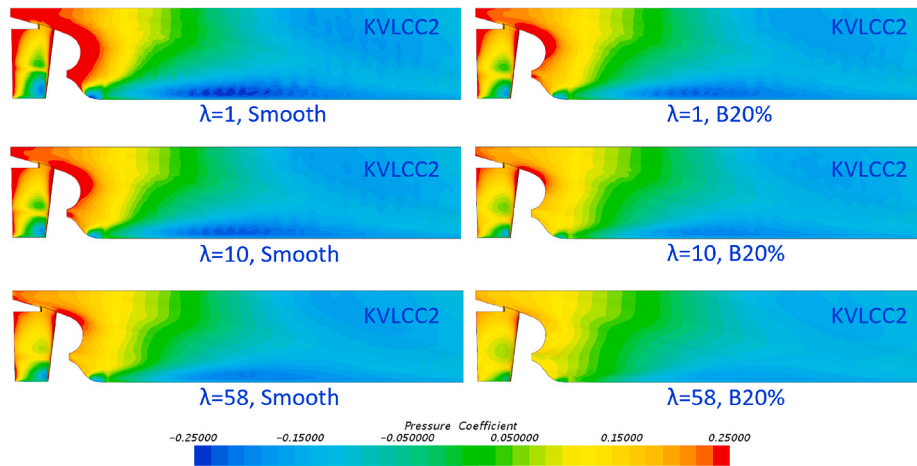


Fig. 25. Pressure coefficient on stern region of KVLCC2 in different scales with smooth and B20% surface conditions.

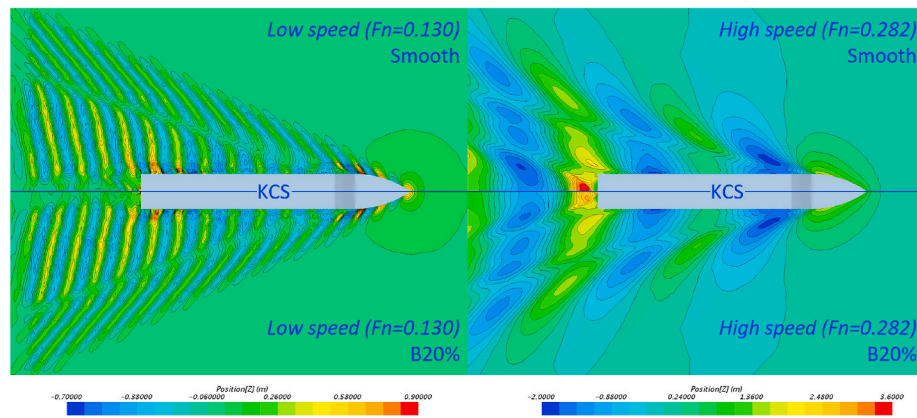


Fig. 26. wave pattern around KCS hulls at low speed (left) and high speed (right) with smooth hull surface (upper of the ship centre line) and fouled (B20%) hull surface (lower of the ship centre line) conditions.

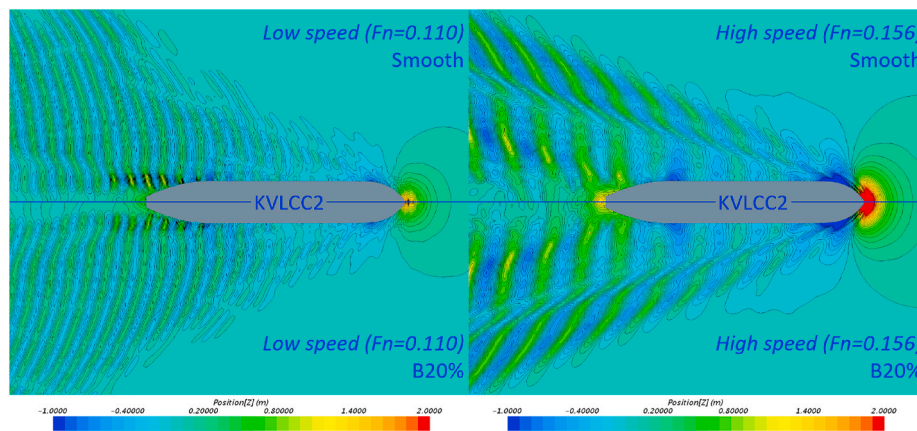


Fig. 27. wave pattern around KVLCC2 hulls at low speed (left) and high speed (right) with smooth surface (upper of the ship centre line) and fouled (B20%) hull surface (lower of the ship centre line) conditions.

Declaration of competing interest

The authors declare that they have no known competing financial interests or personal relationships that could have appeared to influence the work reported in this paper.

Acknowledgements

The authors gratefully acknowledge that the research presented in this paper was carried out as part of the EU funded H2020 project, VENTuRE (grant no. 856887).

It is acknowledged that the results reported in this study were obtained using the ARCHIE-WeSt High-Performance Computer (www.

archie-west.ac.uk) based at the University of Strathclyde.

References

- Atlar, M., Yeginbayeva, I.A., Turkmen, S., Demirel, Y.K., Carchen, A., Marino, A., Williams, D., 2018. A rational approach to predicting the effect of fouling control systems on “in-service” ship performance. *GMO SHIPMAR* 24 (213), 5–36.
- Carchen, A., Atlar, M., Turkmen, S., Pazouki, K., Murphy, A.J., 2019. Ship performance monitoring dedicated to biofouling analysis: development on a small size research catamaran. *Appl. Ocean Res.* 89, 224–236. <https://doi.org/10.1016/j.apor.2019.05.005>.
- Celik, I.B., Ghia, U., Roache, P.J., Freitas, C.J., Coleman, H., Raad, P.E., 2008. Procedure for estimation and reporting of uncertainty due to discretization in CFD applications. *J. Fluid Eng.* 130 (7), 78001. <https://doi.org/10.1115/1.2960953>, 78001-078004.
- Demirel, Y.K., Khorasanchi, M., Turan, O., Incecik, A., Schultz, M.P., 2014. A CFD model for the frictional resistance prediction of antifouling coatings. *Ocean. Eng.* 89, 21–31. <https://doi.org/10.1016/j.oceaneng.2014.07.017>.
- Demirel, Y.K., Song, S., Turan, O., Incecik, A., 2019. Practical added resistance diagrams to predict fouling impact on ship performance. *Ocean. Eng.* 186, 106112. <https://doi.org/10.1016/j.oceaneng.2019.106112>.
- Demirel, Y.K., Turan, O., Incecik, A., 2017b. Predicting the effect of biofouling on ship resistance using CFD. *Appl. Ocean Res.* 62, 100–118. <https://doi.org/10.1016/j.apor.2016.12.003>.
- Demirel, Y.K., Uzun, D., Zhang, Y., Fang, H.-C., Day, A.H., Turan, O., 2017a. Effect of barnacle fouling on ship resistance and powering. *Biofouling* 33 (10), 819–834. <https://doi.org/10.1080/08927014.2017.1373279>.
- Dogrul, A., Song, S., Demirel, Y.K., 2020. Scale effect on ship resistance components and form factor. *Ocean. Eng.* 209, 107428. <https://doi.org/10.1016/j.oceaneng.2020.107428>.
- Farkas, A., Degiuli, N., Martić, I., 2018. Towards the prediction of the effect of biofilm on the ship resistance using CFD. *Ocean. Eng.* 167, 169–186. <https://doi.org/10.1016/j.oceaneng.2018.08.055>.
- Farkas, A., Degiuli, N., Martić, I., 2019. Impact of biofilm on the resistance characteristics and nominal wake. *Proc. IME M J. Eng. Marit. Environ.* <https://doi.org/10.1177/1475090219862897>, 1475090219862897.
- Farkas, A., Degiuli, N., Martić, I., 2020b. An investigation into the effect of hard fouling on the ship resistance using CFD. *Appl. Ocean Res.* 100, 102205. <https://doi.org/10.1016/j.apor.2020.102205>.
- Farkas, A., Song, S., Degiuli, N., Martić, I., Demirel, Y.K., 2020a. Impact of biofilm on the ship propulsion characteristics and the speed reduction. *Ocean. Eng.* 199, 107033. <https://doi.org/10.1016/j.oceaneng.2020.107033>.
- Flack, K.A., Schultz, M.P., 2010. Review of hydraulic roughness scales in the fully rough regime. *J. Fluid Eng.* 132 (4), 41203–41210. <https://doi.org/10.1115/1.4001492>, 041203.
- García Gomez, A., 2000. On the form factor scale effect. *Ocean. Eng.* 27 (1), 97–109. [https://doi.org/10.1016/S0029-8018\(98\)00042-0](https://doi.org/10.1016/S0029-8018(98)00042-0).
- Granville, P.S., 1958. The frictional resistance and turbulent boundary layer of rough surfaces. *J. Ship Res.* 2 (3), 52–74.
- Granville, P.S., 1978. Similarity-law characterization methods for arbitrary hydrodynamic roughnesses. In: Granville, P.S. (Ed.), *Final Report Naval Ship Research and Development Center*, Bethesda, MD. Ship Performance Dept. David Taylor Naval Ship Research and Development Center, Bethesda, MD, p. 31.
- Grigson, C., 1992. Drag losses of new ships caused by hull finish. *J. Ship Res.* 36, 182–196.
- Kim, W.J., Van, S.H., Kim, D.H., 2001. Measurement of flows around modern commercial ship models. *Exp. Fluids* 31 (5), 567–578. <https://doi.org/10.1007/s003480100332>.
- Larsson, L., Stern, F., Visonneau, M., 2013. CFD in ship hydrodynamics—results of the gothenburg 2010 workshop. In: Eça, L., Oñate, E., García-Espinosa, J., Kvamsdal, T., Bergan, P. (Eds.), *MARINE 2011, IV International Conference on Computational Methods in Marine Engineering: Selected Papers*. Springer, Dordrecht, pp. 237–259 (Netherlands).
- Lewis, E.V., 1988. *Principles of Naval Architecture: Resistance, Propulsion and Vibration: 2*. The Society of Naval Architects and Marine Engineers, Jersey City.
- Li, C., Atlar, M., Haroutunian, M., Norman, R., Anderson, C., 2019. An investigation into the effects of marine biofilm on the roughness and drag characteristics of surfaces coated with different sized cuprous oxide (Cu₂O) particles. *Biofouling* 1–19. <https://doi.org/10.1080/08927014.2018.1559305>.
- Menter, F.R., 1994. Two-equation eddy-viscosity turbulence models for engineering applications. *AIAA J.* 32 (8), 1598–1605.
- Moody, L.F., 1944. Friction factors for pipe flow. *Friction factors for pipe flow*. *Trans. Am. Soc. Mech. Eng.* 66, 671–681.
- Min, K.-S., Kang, S.-H., 2010. Study on the form factor and full-scale ship resistance prediction method. *J. Mar. Sci. Technol.* 15 (2), 108–118. <https://doi.org/10.1007/s00773-009-0077-y>.
- Owen, D., Demirel, Y.K., Oguz, E., Tezdogan, T., Incecik, A., 2018. Investigating the effect of biofouling on propeller characteristics using CFD. *Ocean Engineering*. doi: <https://doi.org/10.1016/j.oceaneng.2018.01.087>.
- Schultz, M.P., 2002. The relationship between frictional resistance and roughness for surfaces smoothed by sanding. *J. Fluid Eng.* 124 (2), 492–499. <https://doi.org/10.1115/1.1459073>.
- Schultz, M.P., 2004. Frictional resistance of antifouling coating systems. *J. Fluid Eng.* 126 (6), 1039–1047. <https://doi.org/10.1115/1.1845552>.
- Schultz, M.P., Bendick, J.A., Holm, E.R., Hertel, W.M., 2011. Economic impact of biofouling on a naval surface ship. *Biofouling* 27 (1), 87–98. <https://doi.org/10.1080/08927014.2010.542809>.
- Schultz, M.P., Flack, K.A., 2007. The rough-wall turbulent boundary layer from the hydraulically smooth to the fully rough regime. *J. Fluid Mech.* 580, 381–405. <https://doi.org/10.1017/S0022112007005502>.
- Siemens, 2018. STAR-CCM+, user guide, version 13.06.
- Song, S., Dai, S., Demirel, Y.K., Atlar, M., Day, S., Turan, O., 2020d. E xperimental and theoretical study of the effect of hull roughness on ship resistance. *Journal of Ship Research* (accepted/in press).
- Song, S., Demirel, Y.K., Atlar, M., 2019a. An Investigation into the Effect of Biofouling on Full-Scale Propeller Performance Using CFD. Paper Presented at the 38th International Conference on Ocean, Offshore & Arctic Engineering, Glasgow.
- Song, S., Demirel, Y.K., Atlar, M., 2019b. An investigation into the effect of biofouling on the ship hydrodynamic characteristics using CFD. *Ocean. Eng.* 175, 122–137. <https://doi.org/10.1016/j.oceaneng.2019.01.056>.
- Song, S., Demirel, Y.K., Atlar, M., 2020b. Penalty of hull and propeller fouling on ship self-propulsion performance. *Appl. Ocean Res.* 94, 102006. <https://doi.org/10.1016/j.apor.2019.102006>.
- Song, S., Demirel, Y.K., Atlar, M., Dai, S., Day, S., Turan, O., 2020c. Validation of the CFD approach for modelling roughness effect on ship resistance. *Ocean. Eng.* 200, 107029. <https://doi.org/10.1016/j.oceaneng.2020.107029>.
- Song, S., Demirel, Y.K., Atlar, M., 2020a. Propeller performance penalty of biofouling: computational fluid dynamics prediction. *J. Offshore Mech. Arctic Eng.* 142 (6) <https://doi.org/10.1115/1.4047201>.
- Terziev, M., Tezdogan, T., Incecik, A., 2019b. Application of eddy-viscosity turbulence models to problems in ship hydrodynamics. *Ships Offshore Struct.* 1–24. <https://doi.org/10.1080/17445302.2019.1661625>.
- Terziev, M., Tezdogan, T., Incecik, A., 2019a. A geosim analysis of ship resistance decomposition and scale effects with the aid of CFD. *Appl. Ocean Res.* 92, 101930. <https://doi.org/10.1016/j.apor.2019.101930>.
- Terziev, M., Tezdogan, T., Oguz, E., Gourlay, T., Demirel, Y.K., Incecik, A., 2018. Numerical investigation of the behaviour and performance of ships advancing through restricted shallow waters. *J. Fluid Struct.* 76, 185–215. <https://doi.org/10.1016/j.jfluidstructs.2017.10.003>.
- Terziev, M.Z.G., Tezdogan, T., Yuan, Z., Incecik, A., 2020. Virtual replica of a towing tank experiment to determine the Kelvin half-angle of a ship in restricted water. *J. Mar. Sci. Eng.* 8 (4), 258.
- Tezdogan, T., Demirel, Y.K., 2014. An overview of marine corrosion protection with a focus on cathodic protection and coatings. *Brodogradnja* 65, 49–59.
- Tezdogan, T., Demirel, Y.K., Kellett, P., Khorasanchi, M., Incecik, A., Turan, O., 2015. Full-scale unsteady RANS CFD simulations of ship behaviour and performance in head seas due to slow steaming. *Ocean. Eng.* 97, 186–206. <https://doi.org/10.1016/j.oceaneng.2015.01.011>.
- Townsin, R.L., 2003. The ship hull fouling penalty. *Biofouling* 19 (Suppl. 1), 9–15. <https://doi.org/10.1080/0892701031000088535>.
- Uzun, D., Demirel, Y.K., Coraddu, A., Turan, O., 2019. Time-dependent biofouling growth model for predicting the effects of biofouling on ship resistance and powering. *Ocean. Eng.* 191, 106432. <https://doi.org/10.1016/j.oceaneng.2019.106432>.
- Uzun, D., Ozyurt, R., Demirel, Y.K., Turan, O., 2020. Does the barnacle settlement pattern affect ship resistance and powering? *Appl. Ocean Res.* 95, 102020. <https://doi.org/10.1016/j.apor.2019.102020>.
- Van, S.-H., Ahn, H., Lee, Y.-Y., Kim, C., Hwang, S., Kim, J., Kim, K.-S., Park, I.-R. (vol. 2011, 4–6 April). Resistance Characteristics and Form Factor Evaluation for Geosim Models of KVLCC2 and KCS. Paper Presented at the 2nd International Conference on Advanced Model Measurement Technology for the EU Maritime Industry, Newcastle upon Tyne, UK.